

ABSENCE OF FAST-MOVING IRON IN AN INTERMEDIATE TYPE Ia SUPERNOVA BETWEEN NORMAL AND SUPER-CHANDRASEKHAR

YI CAO¹, J. JOHANSSON², PETER E. NUGENT^{3,4}, A. GOOBAR⁵, JAKOB NORDIN⁶, S. R. KULKARNI¹, S. BRADLEY CENKO^{7,8}, ORI D. FOX^{4,9}, MANSI M. KASLIWAL^{1,10}, C. FREMLING¹¹, R. AMANULLAH⁵, E. Y. HSIAO^{12,13}, D. A. PERLEY¹, BRIAN D. BUE¹⁴, FRANK J. MASCI¹⁵, WILLIAM H. LEE¹⁶, NICOLAS CHOTARD¹⁷

Draft version March 2, 2022

ABSTRACT

In this paper, we report observations of a peculiar Type Ia supernova iPTF13asv (a.k.a., SN2013cv) from the onset of the explosion to months after its peak. The early-phase spectra of iPTF13asv show absence of iron absorption, indicating that synthesized iron elements are confined to low-velocity regions of the ejecta, which, in turn, implies a stratified ejecta structure along the line of sight. Our analysis of iPTF13asv's light curves and spectra shows that it is an intermediate case between normal and super-Chandrasekhar events. On the one hand, its light curve shape (B-band $\Delta m_{15} = 1.03 \pm 0.01$) and overall spectral features resemble those of normal Type Ia supernovae. On the other hand, similar to super-Chandrasekhar events, it shows large peak optical and UV luminosity ($M_B = -19.84$ mag, $M_{uvm2} = -15.5$ mag) a relatively low but almost constant Si II velocities of about 10,000 km s⁻¹, and persistent carbon absorption in the spectra. We estimate a ⁵⁶Ni mass of $0.81^{+0.10}_{-0.18} M_{\odot}$ and a total ejecta mass of $1.59^{+0.45}_{-0.12} M_{\odot}$. The large ejecta mass of iPTF13asv and its stratified ejecta structure together seemingly favor a double-degenerate origin.

Subject headings: supernovae: general – supernovae: individual (iPTF13asv, SN2013cv) – ultraviolet: general

1. INTRODUCTION

Type Ia supernovae (SNe) are thermonuclear explosions of carbon-oxygen white dwarfs (WDs). Since the majority of them (the normal Type SNe Ia) follow a well-

established empirical relation between variation of their peak magnitudes and light curve shapes (Phillips 1993), they are standardized to measure cosmological distances (see Goobar & Leibundgut 2011 for a review). However, the underlying progenitor systems and explosion mechanisms of SNe Ia remain poorly understood.

Recent observations have provided mounting evidence that SNe Ia have multiple progenitor channels (see Maoz et al. 2014 for a review). In the single-degenerate (SD) channel, a WD accretes material from a companion star and explodes when its mass approaches the Chandrasekhar limit (Whelan & Iben 1973). This channel is supported by possible detections of companion stars in pre- or post-SN images (McCully et al. 2014; Foley et al. 2014), likely signatures of SN-companion collisions (Cao et al. 2015; Marion et al. 2016), and observations of variable Na I D absorption (Patat et al. 2007; Sternberg et al. 2014). In the double-degenerate (DD) channel, in contrast, two WDs collide or merge in a binary or even triple system to produce a SN Ia (e.g., Nomoto & Iben 1985; Kushnir et al. 2013). This channel is consistent with observations of two nearby Type Ia SN2011fe and SN2014J (e.g., Li et al. 2011; Brown et al. 2012; Shappee et al. 2013; Margutti et al. 2014; Kelly et al. 2014; Goobar et al. 2015; Lundqvist et al. 2015). Despite these interesting constraints from individual events, the progenitors of most SNe Ia are still unknown.

In the SD channel, rigid rotation may provide additional support for a WD of a mass slightly larger than the Chandrasekhar limit and differential rotation may support for an even more massive WD. However, the theoretical viability of massive, rotation-supported WDs is much less clear in reality (Yoon & Langer 2004; Saio & Nomoto 2004; Piro 2008; Justham 2011; Di Stefano et al. 2011; Hachisu et al. 2012). In the DD channel, in

¹ Astronomy Department, California Institute of Technology, Pasadena, CA 91125, USA

² Ben-Zvi Center for Astrophysics, Weizmann Institute of Science, 76100 Rehovot, Israel

³ Computational Cosmology Center, Computational Research Division, Lawrence Berkeley National Laboratory, 1 Cyclotron Road, MS 50B-4206, Berkeley, CA 94720, USA

⁴ Department of Astronomy, University of California Berkeley, Berkeley, CA 94720-3411, USA

⁵ Oskar Klein Centre, Physics Department, Stockholm University, SE-106 91 Stockholm, Sweden

⁶ Institut für Physik, Humboldt-Universität zu Berlin, Newtonstr. 15, 12489 Berlin, Germany

⁷ Astrophysics Science Division, NASA Goddard Space Flight Center, Mail Code 661, Greenbelt, Maryland 20771, USA

⁸ Joint Space-Science Institute, University of Maryland, College Park, MD 20742, USA

⁹ Space Telescope Science Institute, 3700 San Martin Drive, Baltimore, MD 21218, USA

¹⁰ Observatories of the Carnegie Institution for Science, 813 Santa Barbara Street, Pasadena, California 91101, USA

¹¹ Department of Astronomy, The Oskar Klein Center, Stockholm University, AlbaNova, 10691 Stockholm, Sweden

¹² Department of Physics, Florida State University, Tallahassee, FL 32306, USA

¹³ Department of Physics and Astronomy, Aarhus University, Ny Munkegade 120, 8000 Aarhus C, Denmark

¹⁴ Jet Propulsion Laboratory, California Institute of Technology, Pasadena, CA 91125, USA

¹⁵ Infrared Processing and Analysis Center, California Institute of Technology, MS 100-22, Pasadena, CA 91125, USA

¹⁶ Instituto de Astronomía, Universidad Nacional Autónoma de México, Apdo. Postal 70-264 Cd. Universitaria, México DF 04510, México

¹⁷ Université de Lyon, F-69622, France ; Université de Lyon 1, Villeurbanne ; CNRS/IN2P3, Institut de Physique Nucléaire de Lyon

contrast, the exploding WD binary may allow SN ejecta mass much higher than the Chandrasekhar limit. In fact, more than a handful of SNe were found to have total ejecta masses significantly exceeding the Chandrasekhar limit (Howell et al. 2006; Hicken et al. 2007; Yuan et al. 2010; Yamanaka et al. 2009; Scalzo et al. 2010; Silverman et al. 2011; Scalzo et al. 2014c). However, these super-Chandrasekhar SNe show distinctive characteristics compared to normal events: they are overluminous in both the optical and UV, implying a large amount of synthesized ^{56}Ni . They show low expansion velocities and long rise times, leading to massive ejecta. They also show persistent absorption from unburned carbon.

In this paper, we present observations of a peculiar SN Ia, iPTF13asv, which shares observational characteristics with both super-Chandrasekhar and normal SN Ia. It was discovered with $r = 20.54 \pm 0.16$ mag at $\alpha = 16^{\text{h}}22^{\text{m}}43^{\text{s}}.19$, $\delta = +18^{\circ}57'35''.0$ (J2000) in the vicinity of galaxy SDSS J162243.02+185733.8 on UTC 2013 May 1.44 (hereafter May 1.44) by the intermediate Palomar Transient Factory (iPTF; Law et al. 2009; Rau et al. 2009). Nothing was seen at the same location down to $5\text{-}\sigma$ detection thresholds of $r \simeq 21.0$ mag on images taken on April 30.5 and earlier. iPTF13asv was independently discovered and classified as a peculiar type Ia by Zhou et al. (2013), and was designated as SN2013cv.

This paper is organized as follows: the observational data are presented in §2. The photometric and spectroscopic properties are analyzed in §3, and we construct its bolometric light curve and estimate the total ejecta mass in §4. A discussion of the nature of iPTF13asv is given in §5 and our conclusions are summarized in §6.

In order to have a comparison to other SNe, we adopt a fiducial value of the Hubble constant $H_0 = 72 \text{ km s}^{-1} \text{ Mpc}^{-1}$. The apparent host galaxy of iPTF13asv does not have a redshift-independent distance measurement in the NASA/IPAC Extragalactic Database. Thus the redshift 0.036 leads to a distance modulus of 35.94 mag. The peculiar motion of the host galaxy at $\sim 100 \text{ km s}^{-1}$ introduces an uncertainty of $\lesssim 0.05$ mag to the distance modulus. The Galactic line-of-sight extinction is $E(B - V) = 0.045$ (Schlafly & Finkbeiner 2011). We correct for the Galactic extinction by using the parameterized model in Fitzpatrick (1999) with $R_V = 3.1$.

2. OBSERVATIONS

The nightly cadence survey of iPTF (weather permitting) with the 48-inch telescope at the Palomar Observatories (P48) provides a well-sampled R-band light curve of iPTF13asv covering the pre-SN history and its rise phase. After discovery, we also utilized the Palomar 60-inch telescope (P60; Cenko et al. 2006), the Andalusia Faint Object Spectrograph and Camera (ALFOSC) on the Nordic Optical Telescope (NOT), and the RATIR camera mounted on the OAN/SPM 1.5-meter Harold L. Johnson telescope for multi-band photometric follow-up observations. We also triggered target-of-opportunity observations of the *Swift* spacecraft for X-ray and UV follow-up. The ground-based photometric measurements are presented in Table 1 and the space-based measurements in Table 2.

Spectroscopic observations were undertaken with the

Table 1
Photometry of iPTF13asv

Tel./Inst. ¹	Filter (day)	MJD−56000	mag. ²	mag. err.
P48	PTF-R	412.456	>20.35	...
P48	PTF-R	413.442	20.44	0.17
P48	PTF-R	413.471	20.34	0.16
P48	PTF-R	414.470	19.58	0.09
P48	PTF-R	415.469	19.06	0.06
		...		

¹ This column lists the telescopes and instruments used for photometric observations of iPTF13asv. We built reference images by stacking pre-SN or post-SN frames and used an image subtraction technique to remove light contamination from the host galaxy. Point-spread function (PSF) photometry is performed on subtracted images. The photometry is calibrated either to SDSS or by observing Landolt photometric standard stars.

² Conventionally, the magnitudes in *UBVJH* bands are in the Vega system. Those in other bands are in the AB system. No extinction is corrected in this column.

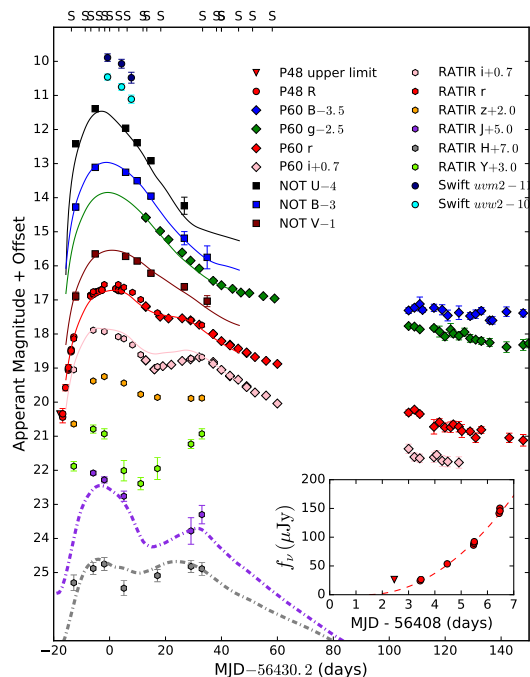


Figure 1. Multi-color light curve of iPTF13asv. Colors and shapes represent different filters and instruments, respectively. A deviation of $\simeq 0.1$ mag between the P48 R-band (red circles) and P60 r-band (red diamonds) is due to the difference between the P48 Mould R filter and the P60 SDSS r filter. The “S” ticks on the top axis denote spectroscopic observation epochs. The solid curves are SALT2 best-fit light curves in corresponding filters. The dashed-dotted curves are the IR template from Stanishv et al. (2015). The inset zooms into the very early phases of the PTF R-band light curve. The dashed curve in the inset shows the best t^2 law fit to the early light curve.

SN Integral Field Spectrograph (SNIFS; Lantz et al. 2004) on the 2.2 m telescope of the University of Hawaii, the Dual Imaging Spectrograph (DIS) on the ARC 3.5 m telescope at Apache Point Observatory (APO), the Double Spectrograph (DBSP; Oke & Gunn 1982) on the 200-

Table 2
Swift Observations

Obs. Date	UVOT/ <i>uvm2</i> ¹		UVOT/ <i>uvw2</i> ¹		XRT ²	
	exp. time (s)	mag (AB)	exp. time (s)	mag (AB)	exp. time (s)	counts (cnts s ⁻¹)
May 17.4	1386	21.02 ± 0.08	1540	20.59 ± 0.08	2971	< 3.6 × 10 ⁻³
May 22.6	1154	21.25 ± 0.10	1193	20.92 ± 0.09	2382	< 8.0 × 10 ⁻³
May 25.9	1298	21.83 ± 0.12	1274	21.39 ± 0.10	2625	< 4.3 × 10 ⁻³
June 02.7	646	< 22.20	604	< 22.36	1264	< 9.0 × 10 ⁻³
June 10.5	462	< 21.98	464	< 22.18	928	< 1.2 × 10 ⁻²
June 13.4	612	< 22.37	674	< 22.46	1326	< 8.7 × 10 ⁻³

¹ We used the `HEASoft` package to perform aperture photometry on the UVOT images. The photometry is corrected for coincident loss and with the PSF growth curve and calibrated with the latest calibration (Breeveld et al. 2011). In order to remove host galaxy contamination in the photometric measurements, we acquired post-SN reference frames. In cases of non-detection, we estimated 3- σ upper limits.

² We used the `XImage` software to analyze the XRT data. In cases of non-detection, we estimate upper limits with a 99.7% confidence level.

inch Hale telescope (P200) at Palomar Observatory, and the Folded-port InfraRed Echellette (FIRE) on the Magellan Baade Telescope at Las Campanas Observatory. The spectral sequence is presented in Figure 2.

The light curves and spectra are made publicly available via WISEREP¹⁸ (Yaron & Gal-Yam 2012).

3. ANALYSIS

3.1. Initial Rise and Explosion Date

In order to determine the explosion date of iPTF13asv, we follow Nugent et al. (2011) and model the early PTF R-band light curve of iPTF13asv as a freely expanding fireball where the luminosity increases as $\propto t^2$ and the temperature remains constant. Restricting ourselves to the light curve within four days of discovery, we find a best fit (the inset in Figure 1) at an explosion date of April 29.4 ± 0.3 (95% confidence interval) with a fitting $\chi^2 = 4.3$ for five degrees of freedom. The best-fit light curve is also consistent with the non-detection upper limit on April 30.4.

If we generalize the t^2 model with a power-law model, we obtain strong degeneracy between the explosion date and the power-law index over a large range of the parameter space. In fact, Firth et al. (2015) analyzed the rise behavior of a large sample of SNe Ia with the power-law model and also found that the power-law indices have large uncertainties with a mean value of 2.5. This is probably because shallow-deposited ⁵⁶Ni heats up SN photospheres. Furthermore, there could be a dark time between the SN explosion and the SN light curve powered by radioactive decay on the diffusive timescale for the shallowest deposition of ⁵⁶Ni in the ejecta (Piro 2012; Piro & Morozova 2015). Hence, it is nontrivial to estimate the exact explosion date purely from the early light curve. Since the following analysis and discussion are not very sensitive to the exact explosion date, for simplicity, we adopt the explosion date determined by the t^2 model.

3.2. Absence of Iron in Early-phase Spectra

The most striking feature of these early-phase spectra is the absence of iron absorption. We used SYN++ (Thomas et al. 2011a) to perform spectral feature identification on the spectrum taken 11 days after explosion

(or equivalently, -13.7 days with respect to the B-band maximum which is determined in §3.3). As highlighted in gray in Figure 3, the spectrum shows no signature of either Fe II or Fe III.

We also compare early-phase spectra of iPTF13asv to those of well-studied normal and overluminous Type Ia events in the top panels of Figure 4. Most spectra in comparison, including the spectrum of the super-Chandrasekhar SN2009dc at -7 days, clearly show the existence of iron absorption features. The exceptions are two super-Chandrasekhar events, SN2006gz and SN2007if, which have weak or no iron absorption.

As a result of nucleosynthesis and mixing during SN explosions, iron commonly manifests itself as absorption features in SN spectra, either as Fe II at low effective temperatures or as Fe III at higher temperatures. The absence of iron at early phases implies that weak mixing during the SN explosion confines synthesized iron group elements in low-velocity regions of the ejecta.

The centric concentration of iron can be verified by strong UV emission at the same time, as the iron group elements are the main absorbers of photons below 3500 Å. However, we did not trigger *Swift* observations at early phases because the SN is located beyond our trigger criteria of 100 Mpc. In comparison to the spectral shape of SN2011fe, the spectral shape of iPTF13asv at -7 days (top right panel of Figure 4) indicates stronger fluxes at shorter wavelengths, hinting a strong emission in the UV.

The weak mixing of iron in the SN explosion may have strong implications for the explosion mechanism and will be discussed in §5.3. As shown in the bottom two panels of Figure 4, iron features appear in the iPTF13asv spectra around and after maximum. In the next few subsections, we investigate the specifics of iPTF13asv.

3.3. Light Curves

In order to determine the light curve shape parameters of iPTF13asv, we use the SALT2 software (Guy et al. 2007) to fit its optical light curve (see Figure 1 for the SALT2 best-fit light curves). The best-fit light curve gives a rest-frame B-band peak magnitude $m_B = 16.28 \pm 0.03$ on May 18.12 ± 0.09. We set this B-band peak date as $t = 0$ in the rest of this paper. The fit also gives a color term $c = -0.16 \pm 0.02$, and two shape parameters

¹⁸ WISEREP is available at <http://www.weizmann.ac.il/astrophysics/wiserep/>.

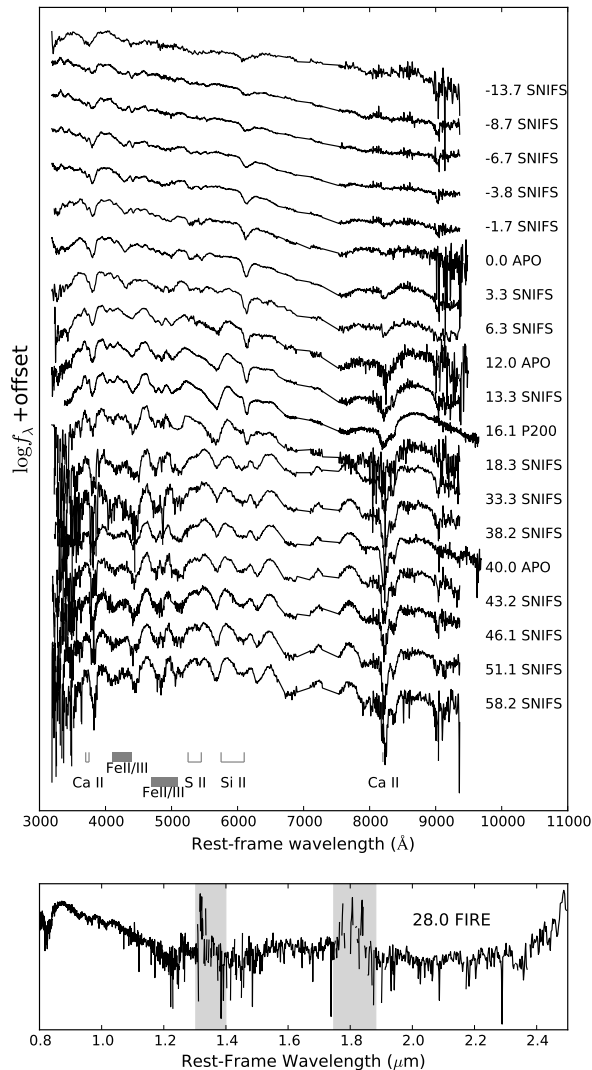


Figure 2. Optical and near-IR spectral evolution of iPTF13asv. Ticks at the bottom denote the main spectral features. The phases and telescopes/instruments are labeled to the right of corresponding spectra. The long-slit spectra taken by APO/DIS, P200/DBSP and Magellan/FIRE are extracted through the usual procedures in IRAF and/or IDL and calibrated using observations of spectroscopic flux standard stars. Data reduction of SNIFS is outlined in Aldering et al. (2006). However, due to bad weather, flux calibration of SNIFS spectra was not complete. Therefore, we interpolate the multi-band light curves and “warp” the spectra with low-order polynomials to match photometric data.

$x_0 = 0.0055 \pm 0.0001$ and $x_1 = 0.37 \pm 0.09$. Based on the fitted SALT2 light curve, we derive a color $(B - V)_0 = -0.14 \pm 0.03$ at the B-band maximum. We also obtain $\Delta m_{15} = 1.03 \pm 0.01$ from x_1 by using the relation in Guy et al. (2007).

The local extinction in the host galaxy of iPTF13asv is probably minor for several reasons. First, Figure 5 compares the $B - V$ colors between iPTF13asv ($\Delta m_{15} =$

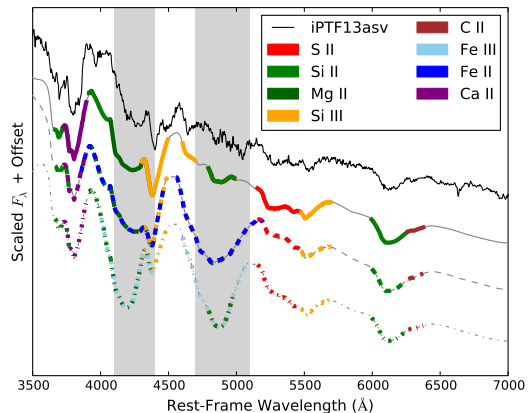


Figure 3. SYN++ synthetic SN spectrum fit to iPTF13asv at -9.2 days. From top to bottom are the observed spectrum, the synthetic spectrum without Fe (solid), the synthetic spectrum with Fe II (dashed), and the synthetic spectrum with Fe III (dashed-dotted). The absorption features from different species are illustrated in different colors. The Fe II and Fe III absorption wavelength ranges are highlighted in light gray.

1.03 mag) and SN2011fe ($\Delta m_{15} = 1.10$ mag). Since SN2011fe is unreddened by its host (Nugent et al. 2011; Vinkó et al. 2012), similar colors around maximum suggest that iPTF13asv also has little local extinction. After the maximum, iPTF13asv has a slightly blue color compared to SN2011fe, probably due to the different stretch of these two events (Nobili & Goobar 2008), until they join the Lira relation after +30 days. Second, the intrinsic color $B - V = 0.95$ mag of iPTF13asv at +35 days is consistent with the latest calibration of the Lira relation (Burns et al. 2014). Third, the absence of Na I D absorption in the low-resolution optical spectra also implies weak extinction in the host galaxy. Given a typical velocity dispersion of 10 km s^{-1} for a dwarf galaxy (see §3.5 for a discussion of the iPTF13asv host galaxy; Walker et al. 2007), we derive from the highest signal-to-noise ratio spectrum that the equivalent width for each of the Na I D lines is less than 0.2 \AA ($5\text{-}\sigma$). Using the empirical relation in Poznanski et al. (2012), we find that the extinction $E(B - V) < 0.06$. Therefore, in what follows, we neglect the local extinction correction.

After correction for Galactic extinction we derive an absolute peak magnitude of iPTF13asv in its rest-frame B-band to be -19.84 ± 0.06 . This is about 0.5 mag brighter than normal SNe Ia at peak.

The k -correction in the UV and optical wavelengths is negligible. Synthetic photometry using both the Nugent SN Ia template (Nugent et al. 2002) and the observed *HST* UV spectra of SN2011fe (Mazzali et al. 2014), shows that the k -correction is less than 0.1 mag in the optical and 0.2 mag in the *Swift*/UVOT UV filters.

In Figure 6, the optical light curves of iPTF13asv are compared to those of well-studied SNe, including normal SN2011fe; overluminous SN1999aa and SN1991T; and super-Chandrasekhar SN2006gz, SN2007if, and SN2009dc. All the light curves have been offset to match their peak magnitudes and to the epoch of the B-band maxima. Figure 6 illustrates that (1) the light curve width of iPTF13asv is similar to those of normal events and narrower than those of overluminous and

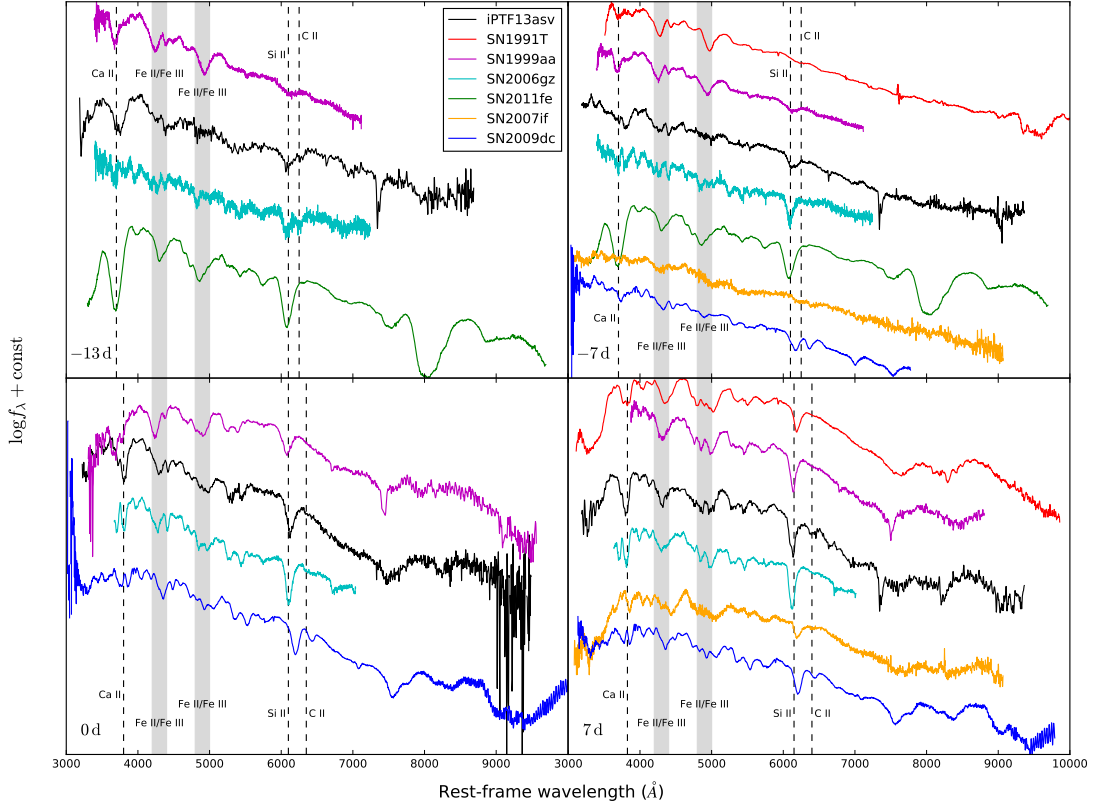


Figure 4. Spectral comparison of iPTF13asv to normal SN2011fe (Pereira et al. 2013); overluminous SN1991T (Mazzali et al. 1995) and SN1999aa (Matheson et al. 2008); and super-Chandrasekhar events SN2006gz (Hicken et al. 2007), SN2007if (Blondin et al. 2012), and SN2009dc (Taubenberger et al. 2011). The phases of the spectra are shown at the lower left corner of each panel.

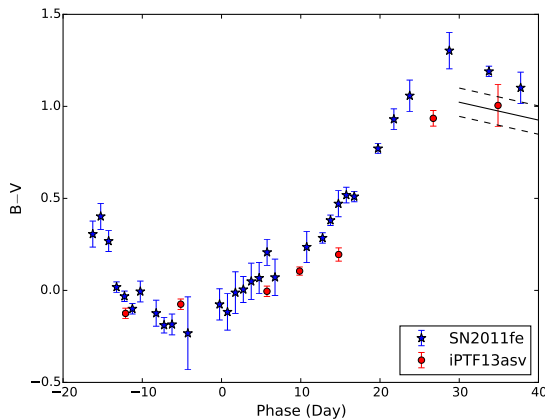


Figure 5. B–V color evolution of SN2011fe and iPTF13asv after correction for Galactic extinction. The solid line shows the Lira relation from Burns et al. (2014) and the dashed lines corresponding to its 0.06 mag scattering.

super-Chandrasekhar events, except for SN2006gz, (2) iPTF13asv shows an isolated secondary maximum in the I-band whose strength is weaker than those observed in SN2011fe and SN1991T, and (3) iPTF13asv matches well

to the super-Chandrasekhar SN2006gz in the B- and V-band light curves, but SN2006gz has a much stronger near-IR secondary peak.

Figure 7 compares iPTF13asv in the *Swift*/UVOT *uvm2* and *uvw2* filters to a large sample of both normal, overluminous, and super-Chandrasekhar SNe Ia observed by *Swift* (Milne et al. 2013; Brown 2014). While the *uvw2* filter has a non-negligible leakage in long wavelengths, the *uvm2* filter does not have a significant leakage and therefore provides the best available measurements of the UV flux. The figure shows that, like super-Chandrasekhar events, iPTF13asv is more luminous in the UV than the majority of normal events. Furthermore, Milne et al. (2013) divided SNe Ia into different subclasses based on their *Swift*/UVOT colors. We cannot make a direct comparison here because only *uvm2* and *uvw2* data are available for iPTF13asv. An indirect comparison is that iPTF13asv is brighter than SN2011fe by half a magnitude in the optical and by $\simeq 0.7$ mag in the UV. Since SN2011fe belongs to the NUV-blue subclass (Brown et al. 2012), iPTF13asv probably also belongs to the same subclass.

We also compare the IR light curves of iPTF13asv in the J- and H-band to the most recent light curve template for normal Type Ia events (Figure 1; Stanishev

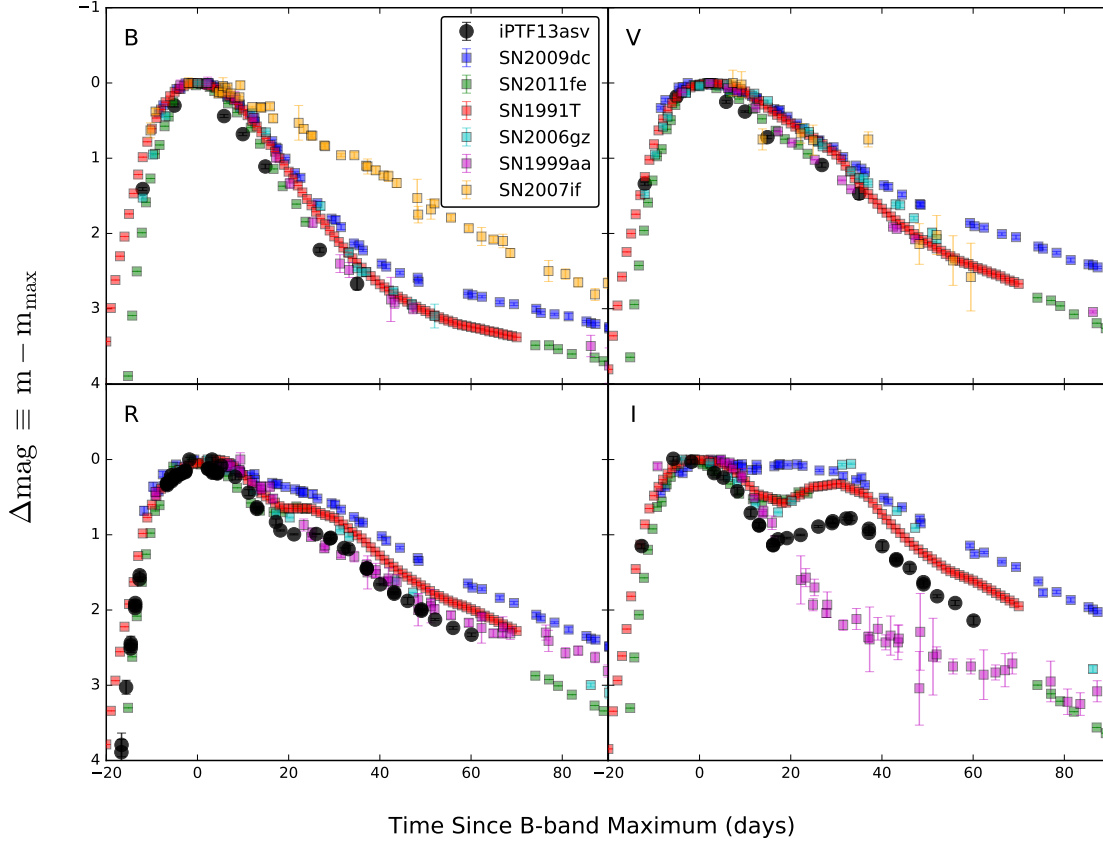


Figure 6. Light curve comparison of iPTF13asv to normal SN2011fe (Pereira et al. 2013); over-luminous SN1991T (Nugent template) and SN1999aa (Krisciunas et al. 2000); and super-Chandrasekhar events SN2006gz (Hicken et al. 2007), SN2007if (Scalzo et al. 2010), and SN2009dc (Silverman et al. 2011). The legend colors are the same as in Figure 4.

et al. 2015) and find that the sparsely sampled light curves of iPTF13asv roughly follow the template. The peak magnitudes of iPTF13asv is $M_J = -18.83 \pm 0.08$ and $M_H = -18.16 \pm 0.19$, compared to the median peak magnitudes of $M_J = -18.39$ and $M_H = -18.36$ with rms scatters of $\sigma_J = 0.116 \pm 0.027$ and $\sigma_H = 0.085 \pm 0.16$ for normal Type Ia SNe (Barone-Nugent et al. 2012). The secondary maximum of iPTF13asv is clearly seen in J-band and H-band light curves as well as the I-band light curve, indicating concentration of iron group elements in the central region of the ejecta (Kasen 2006). This is in accordance with the absence of iron in the outer ejecta.

3.4. Spectra

3.4.1. Spectral Cross-matching

We use the latest versions of both SN Identification (SNID; Blondin & Tonry 2007) and SuperFit (Howell et al. 2005) to spectroscopically classify iPTF13asv. Before -5 days, not surprisingly, neither tools find a good match for iPTF13asv spectra partly because they do not have many early-phase SNe in their templates and partly because the iron absorption is absent in the early-phase spectra of iPTF13asv. Around and after maximum, based on the first 5 best matches, both SNID and SuperFit find that iPTF13asv spectroscopically resem-

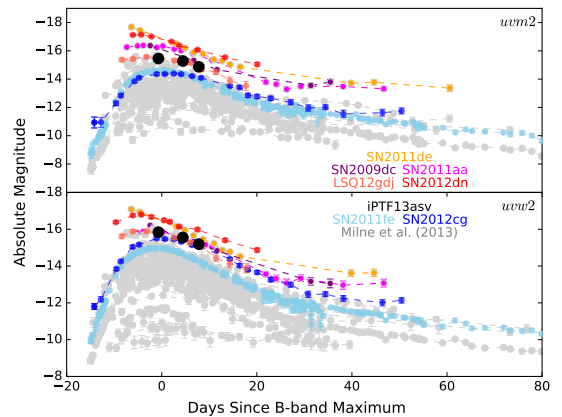


Figure 7. UV light curve comparison between iPTF13asv and other SNe Ia. A sample of SNe Ia from Milne et al. (2013) is shown in gray. Highlighted by different colors are light curves of iPTF13asv (black); SN2011fe (sky blue; Brown et al. 2012); SN2012cg (blue); super-Chandrasekhar events SN2009dc, SN2011aa, and LSQ12gdj (purple; Brown et al. 2014); and the most UV-luminous event SN2011de (orange; Brown 2014). All magnitudes are in the AB system.

bles normal SNe Ia (Table 3).

3.4.2. Spectral comparison to well-studied SNe

Figure 4 compares iPTF13asv spectra to those of well-studied SNe at different epochs: normal SN2011fe (Pereira et al. 2013); overluminous SN1991T (Filippenko et al. 1992) and SN1999aa (Garavini et al. 2004; Matheson et al. 2008); and super-Chandrasekhar SN2006gz (Hicken et al. 2007), SN2007if (Scalzo et al. 2010), and SN2009dc (Taubenberger et al. 2011). At -13 days (top left panel of Figure 4), although both SN2006gz and iPTF13asv have weak or no absorption from iron, iPTF13asv shows strong Ca II H and K absorption but SN2006gz does not. In comparison, both SN1999aa and SN2011fe at similar phases have both strong Ca II and iron absorptions. In addition, the absorption of C II is apparently weaker in iPTF13asv than in SN2006gz.

At a week before maximum (top right panel of Figure 4), except for the prominent absence of iron in iPTF13asv, the overall spectral features of iPTF13asv are similar to those of normal SNe. Unlike the near-absence of Ca II and Si II lines in SN1991T, iPTF13asv shows apparent Ca II and Si II absorption, the strengths of which are weaker than those seen SN1991T. Besides this, its C II feature becomes weaker.

Around maximum (lower left panel of Figure 4), we find good spectral matches between iPTF13asv and SN2011fe. At this epoch, SN1991T is also becoming similar to normal SNe Ia. The strength of Si II absorption in iPTF13asv is between the weak absorption in SN1991T and the strong one in SN2011fe.

One week after maximum (lower right panel of Figure 4), the spectrum of iPTF13asv is very similar to those of normal events, but with strong C II absorption.

3.4.3. Si II velocities

We further measure the expansion velocity evolution of iPTF13asv by fitting a Gaussian kernel to the Si II 6355 line in each spectrum. The continuum is modeled by a linear regression to regions at both sides of the line. Then we fit a linear model to the velocity measurements between -10 and $+10$ days and estimate a velocity of $(1.0 \pm 0.1) \times 10^4 \text{ km s}^{-1}$ and a velocity gradient close to zero at peak.

Figure 8 shows that Si II velocities at maximum versus peak magnitudes. As can be seen in the figure, iPTF13asv has a Si II velocity lower than the majority of normal SNe Ia and similar to super-Chandrasekhar events. Figure 9 compares Si II velocity gradients at maximum versus peak magnitudes. Again, like super-Chandrasekhar events, iPTF13asv has a velocity gradient close to zero, lower than the majority of normal events.

3.4.4. Carbon signatures

We also note that iPTF13asv shows weak but persistent C II absorption features until at least a week after maximum. Figure 10 shows SYN++ fits to iPTF13asv spectra of high signal-to-noise ratios, demonstrating the existence of C II 6580 and C II 7234 lines. The velocities of these C II lines evolve from $\simeq 14,000 \text{ km s}^{-1}$ at -13.7 days to $\simeq 11,000 \text{ km s}^{-1}$ at $+6.3$ days.

About 30% of normal SNe are estimated to reveal the C II 6580 and C II 7234 absorption notches in early

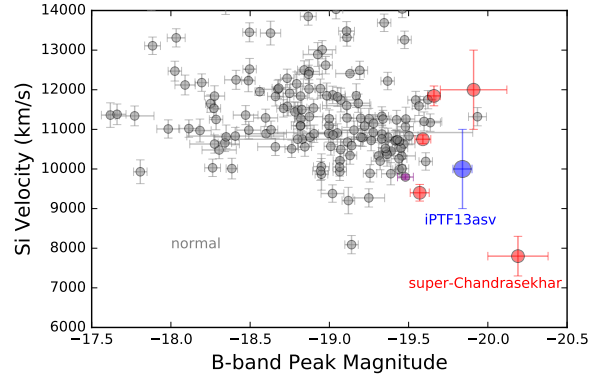


Figure 8. Si II velocities at maximum vs. peak magnitudes. The gray points are measurements taken from Foley et al. (2011) and Scalzo et al. (2014b). Note that Foley et al. (2011) did not correct the local extinction. The red points are taken from Scalzo et al. (2012).

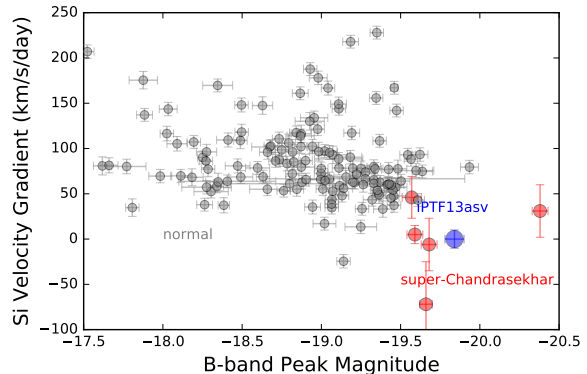


Figure 9. Si II velocity gradients at maximum vs. peak magnitude. The gray points are measurements taken from Foley et al. (2011). Note that Foley et al. (2011) did not correct the local extinction. The red points are taken from Scalzo et al. (2012).

phases (Thomas et al. 2011b; Parrent et al. 2011; Silverman & Filippenko 2012). These C II features usually disappear before maximum. In contrast, some super-Chandrasekhar events show strong and persistent C II features even after maximum. Figure 11 compares the spectra of iPTF13asv at one week after maximum to those of well-studied SNe at similar phases. As can be seen, neither SN1991T nor SN1999aa has the carbon feature at this phase; the carbon signature of iPTF13asv is not as strong as those seen in the super-Chandrasekhar SN2009dc.

3.5. Host Galaxy

After iPTF13asv faded away, we obtained a low signal-to-noise ratio spectrum of its apparent host galaxy SDSS J162254.02+185733.8. The spectrum only shows H α emission at the redshift of iPTF13asv. We fit a Gaussian profile to the H α line and measure a luminosity of $3 \times 10^{38} \text{ erg s}^{-1}$. We adopt the empirical relation between H α luminosity and star formation rate (Kennicutt 1998) and obtain a star formation rate of $2 \times 10^{-3} M_{\odot} \text{ yr}^{-1}$ for the host galaxy.

Next, we construct the spectral energy distribution (SED) of the host galaxy with optical photometry from

Table 3
SNID results

Phase	First Five Best Matches ¹				
-6.8	05eu@-5.2 (normal)	03ic@-4.1 (normal)	08Z@-4.3 (normal)	05na@-1.5 (normal)	06cc@-9.7 (normal)
0.0	96ai@+2.2 (normal)	07F@+3.0 (normal)	94ae@0.0 (normal)	03cg@-2.1 (normal)	94ae@+0.9 (normal)
+6.8	08Z@+7.6 (normal)	05na@+3.4 (normal)	99aa@+1.8 (peculiar)	01fe@+6.2 (normal)	06cz@-2.0 (91T-like)
+13.3	08Z@+12.3 (normal)	07ca@+13.3 (normal)	07bj@+12.0 (normal)	03fa@+13.4 (91T-like)	03kf@+13.4 (normal)

¹ The format in this column is name@phase (subclass).

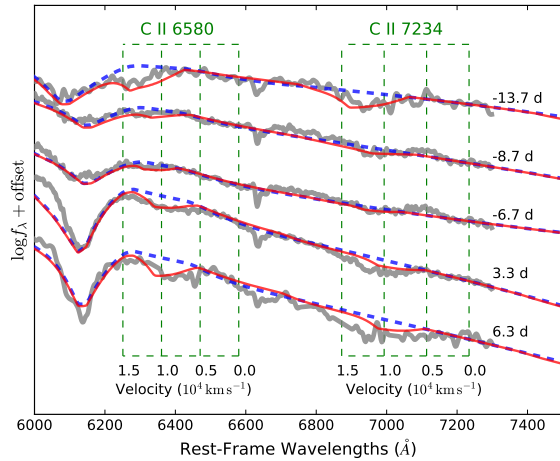


Figure 10. Carbon features of iPTF13asv at different phases. The numbers to the right of each spectrum indicate the phases in days. The observed spectra are shown in gray. The SYN++ spectra without C II are in blue and those with C II are in red. The green dashed axes show velocities of C II 6580 and C II 7234 lines.

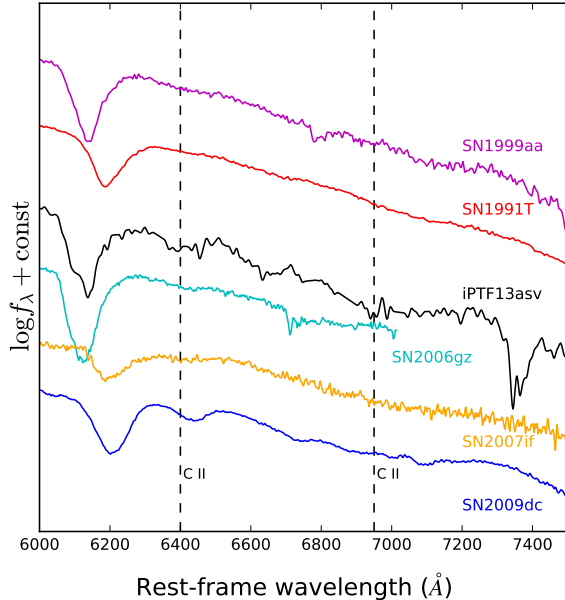


Figure 11. Comparison of carbon features among iPTF13asv, SN1991T, SN1999aa, SN2006gz, SN2007if, and SN2009dc at one week after maximum.

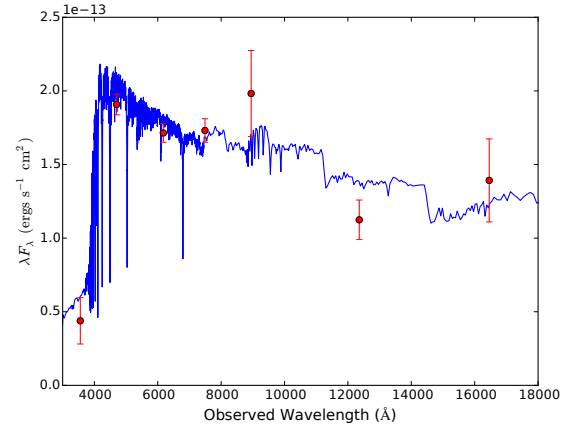


Figure 12. SED fit of the host galaxy. The data points (red) are SDSS model magnitudes in optical and aperture-photometric measurements in the near-IR RATIR reference images. The blue spectrum is the best fit from FAST.

SDSS and near-IR photometry measured on the SN reference images. The SED is then modeled with a galaxy synthesis code called the Fitting and Assessment of Synthetic Templates (Kriek et al. 2009) assuming an exponentially decaying star formation history and a solar metallicity. The best-fit model gives a galaxy age of $10^{8.6}$ years and a stellar mass $\log_{10}(M_{\text{stellar}}/M_{\odot}) = 7.85^{+0.5}_{-0.4}$ with a reduced $\chi^2 = 1.6$ (Figure 12). The best-fit model also shows no ongoing star forming activity. Because SED fitting models are usually insensitive to very low star-forming rates, the best-fit model is consistent with the low star formation rate derived from the $H\alpha$ flux. The derived star formation rate and the stellar mass of the iPTF13asv host galaxy follow the empirical relation between stellar mass and star formation rate (Foster et al. 2012).

Since the host galaxy spectrum does not show [N II] lines, we estimate an upper limit of $\log([\text{N II } 6548/\text{H}\alpha]) < -0.87$. Using Denicoló et al. (2002), we derived a metallicity upper limit of $12 + \log(\text{O}/\text{H}) < 8.3$. In fact, using the mass-metallicity relation (Foster et al. 2012), we estimate a gas-phase metallicity of $12 + \log(\text{O}/\text{H}) \sim 8$ for the host galaxy. Compared to the host galaxy samples of SNe Ia in Pan et al. (2014) and Wolf et al. (2016), SDSS J162254.02+185733.8 is one of the least massive and most metal-poor galaxies that host SNe Ia.

4. BOLOMETRIC LIGHT CURVE AND EJECTA MASS

4.1. Bolometric Light curve

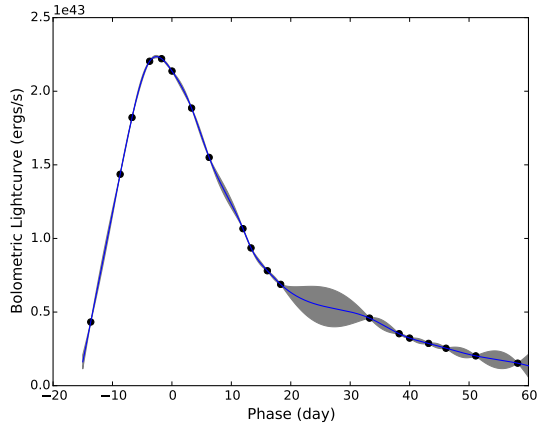


Figure 13. Bolometric light curve. The measured bolometric luminosities at different phases are in black circles. The blue curve is the best fit from the Gaussian process regression. The gray region represents the $1\text{-}\sigma$ uncertainty of the regression curve.

Given the wavelength coverage of the iPTF13asv spectra, we first construct a pseudo-bolometric light curve between 3500 and 9700 Å. In order to calibrate the absolute fluxes of these spectra, we use interpolated optical light curves to “warp” the spectra. Then the spectra are integrated to derive the pseudo-bolometric light curve.

Due to the sparsely sampled UV and IR light curves, it is difficult to estimate the UV and IR radiation at different phases. Therefore we calculate optical-to-bolometric correction factors with a spectral template (Hsiao et al. 2007). In this calculation, we find that the UV correction reaches about 25% before the B-band maximum and quickly drops to less than 5% around and after the B-band maximum. Given the inference that the SN might be UV-luminous before maximum and the observational fact that the SN is among the UV-bright Type Ia SNe around maximum, our calculated correction probably underestimates the UV radiation. Using the *Swift* data around maximum, we estimate that this UV correction introduces a systematic uncertainty of a few percent to the bolometric luminosity. Around maximum when the SN cools down, the UV contribution to the bolometric luminosity becomes even less important.

In the IR, the correction above 9700 Å is below 10% around the B-band maximum, and then reaches a maximum of 24% around the secondary maximum in the near-IR. At the epochs with IR data, we find that the calculated correction is consistent with the IR measurements.

The final bolometric light curve is shown in Figure 13. We further employ Gaussian process regression to derive a maximum bolometric luminosity $L_{max} = (2.2 \pm 0.2) \times 10^{43} \text{ erg s}^{-1}$ at -2.6 days.

4.2. ^{56}Ni Mass and Ejecta Mass

Next, we follow the procedure in Scalzo et al. (2012, 2014a) to derive the ^{56}Ni mass and the total ejecta mass. First, the ^{56}Ni mass can be estimated through the following equation

$$L_{max} = \alpha S(t_R), \quad (1)$$

where $S(t_R)$ is the instantaneous radioactive power at the bolometric luminosity maximum. α is an efficiency

factor of order unity, depending on the distribution of ^{56}Ni (Jeffery et al. 2006). We adopt a fiducial value of $\alpha = 1.3$ following Scalzo et al. (2012). The radioactive power of $^{56}\text{Ni} \rightarrow ^{56}\text{Co} \rightarrow ^{56}\text{Fe}$ is (Nadyozhin 1994)

$$S(t_r) = [6.31 \exp(-t_r/8.8) + 1.43 \exp(-t_r/111)] M_{\text{Ni}}, \quad (2)$$

where $S(t)$ is in units of $10^{43} \text{ erg s}^{-1}$ and M_{Ni} is in units of M_{\odot} . With the measured maximum bolometric luminosity $L_{max} = (2.2 \pm 0.2) \times 10^{43} \text{ erg s}^{-1}$ at -2.6 days, we estimate a ^{56}Ni mass of $(0.77 \pm 0.07) M_{\odot}$.

About one month after the SN maximum, the SN debris expands approximately in a homologous manner. At this time, most ^{56}Ni atoms have decayed to ^{56}Co . Hence the total luminosity can be approximated by

$$L(t) = [1 - \exp(-t_0/t^2)] S_{\gamma}(t) + S_{e+}(t), \quad (3)$$

where S_{γ} and S_{e+} are the decay energy of ^{56}Co carried by γ -ray photons and positrons. At time t_0 , the mean optical path of γ -ray photons becomes unity. For a given density and velocity profile, t_0 reflects the column density along the line of sight. We fit equation (3) to the bolometric light curve of iPTF13asv after +20 days and obtained $t_0 = 44.2 \pm 2.0$ days.

Next, we estimate the total ejecta mass of iPTF13asv. If we assume a density profile $\rho(v) \propto \exp(-v/v_e)$ where v_e is a scale velocity, then the ejecta mass can be expressed as

$$M_{ej} = \frac{8\pi}{\kappa_{\gamma} q} (v_e t_0)^2, \quad (4)$$

where κ_{γ} is the Compton scattering opacity for γ -ray photons. The value of κ_{γ} is expected to lie in the range between 0.025 and $0.033 \text{ cm}^2 \text{ g}^{-1}$ (Swartz et al. 1995). We adopt a value of $0.025 \text{ cm}^2 \text{ g}^{-1}$ for the optically thin regime. The form factor q describes the distribution of ^{56}Ni and thus ^{56}Co (Jeffery 1999). For evenly mixed ^{56}Ni , the value of q is close to one-third. Taking element stratification and mixing in the interfaces into account, Scalzo et al. (2014a) found that $q = 0.45 \pm 0.05$. Here, we adopt $q = 0.45$ in our estimation.

The value of v_e can be obtained by conservation of energy. The total kinetic energy of the ejecta is $6M_{ej}v_e^2$. Neglecting the radiation energy, the total kinetic energy is equal to the difference between the nuclear energy released in the explosion and the binding energy of the exploding WD. The binding energy of a rotating WD with mass M_{ej} and central density ρ_c is given in Yoon & Langer (2005). Here we restrict the central density to lie between 10^7 and $10^{10} \text{ g cm}^{-3}$.

If we further assume that the ejecta is composed of unburned CO and synthesized Si, Fe, and Ni, then the nuclear energy of the SN explosion is formulated in Maeda & Iwamoto (2009) as a function of mass M_{ej} and mass fractions f_{Fe} , f_{Ni} and f_{Si} . The ratio $\eta = f_{\text{Ni}}/(f_{\text{Ni}} + f_{\text{Fe}})$ is also a function of ρ_c . Following Scalzo et al. (2014a), we adopt a Gaussian prior

$$\eta = 0.95 - 0.05\rho_{c,9} \pm 0.03 \max(1, \rho_{c,9}), \quad (5)$$

where $\rho_{c,9}$ is ρ_c in units of 10^9 g cm^{-3} . In addition, we restrict the mass fraction f_{CO} less than 10%.

Based on the above assumptions, with a given set of ejecta mass M_{ej} , central density ρ_c and the mass frac-

tions of different elements, we can calculate the maximum bolometric luminosity and t_0 in equation (3) and compare them with our measurements of iPTF13asv. Here we perform Markov-Chain Monte-Carlo simulations for one million steps and obtain $M_{Ni} = 0.81^{+0.10}_{-0.18}$ and $M_{ej} = 1.44^{+0.44}_{-0.12} M_{\odot}$ at a 95% confidence level.

4.3. Detached Shell Surrounding the SN

In order to explain the almost constant Si II velocity in super-Chandrasekhar events, Scalzo et al. (2010) and Scalzo et al. (2012) hypothesize a stationary shell detached from the ejecta. The shell is accelerated to a constant speed v_{sh} by colliding with fast-moving ejecta with velocities greater than v_{sh} . In fact, some simulations of WD mergers show that the outermost material forms such a stationary envelope that collides with fast-moving ejecta (Hoefflich & Khokhlov 1996). Following the calculation procedure in Scalzo et al. (2010) and Scalzo et al. (2012), we derive an envelope mass of $0.15^{+0.11}_{-0.01} M_{\odot}$ for iPTF13asv. This shell increases the total mass of the system to $1.59^{+0.45}_{-0.12} M_{\odot}$. The ^{56}Ni , shell, and total masses of iPTF13asv are similar to those derived for SN20080522-000 in Scalzo et al. (2012).

The detached shell has little effect on the γ -ray opacity and peak luminosity of an SN. Since the rise time is proportional to $M_{tot}^{1/2}$, the massless detached shell will not make the SN rise substantially longer than usual.

5. DISCUSSIONS

5.1. Origin of Strong UV Emission

Strong UV emission in an SN Ia may be powered by an extrinsic SN-companion collision (Kasen 2010). In fact, in the UV-luminous SN2011de, Brown (2014) offered a possible explanation for its *Swift* light curve as a collision between the SN ejecta and a companion star. Here we consider the same model to interpret the strong UV emission of iPTF13asv.

We utilize the scaling relation in Kasen (2010) to fit the observed *uvm2* light curve. In order to account for the non-negligible emission from the SN itself, we use the well-sampled *uvm2* light curve of SN2011fe as a template. The fitting result shows that the companion star is located at 2×10^{13} cm away from the exploding WD (left panel of Figure 14). Given a typical mass ratio of a few, the companion has a radius of $\sim 100 R_{\odot}$ and fills its Roche lobe.

Although the model fit to the UV light curve looks plausible, it overpredicts the SN emission at very early phases. In the R-band light curve within a few days of explosion, the model-predicted SN flux ($200 \mu\text{Jy}$) is higher than the observed fluxes (the inset of Figure 1) by a factor of $> 30\%$. At -13.7 days, the predicted thermal emission flux from the model below 4000 \AA is also much higher than the observed spectrum (right panel of Figure 14). Hence, we conclude that the strong UV emission seen in iPTF13asv is not produced by SN-companion collision.

As a result of the above analysis, we are forced to conclude that the strong UV emission is intrinsic. In fact, the strong UV emission and the lack of iron in early-phase spectra are probably causally related, as the iron group elements are the major absorbers of UV photons.

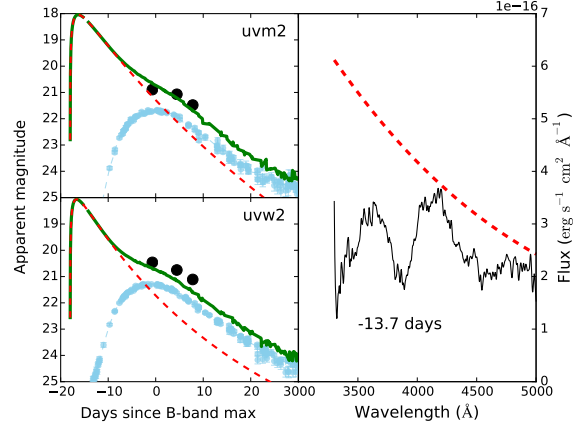


Figure 14. Comparison between the SN-companion interaction signature model and iPTF13asv data. *Left:* the *uvm2* and *uvw2* light curves of iPTF13asv (black circles) are compared to the total light curves (green) which combine the SN-companion interaction component (red; Kasen 2010) and the SN intrinsic emission (cyan). *Right:* the iPTF13asv spectrum at -13.7 days (black) is compared to the thermal spectrum of SN-companion collision (red).

These two observational facts, together with the near-IR secondary peak, strongly suggest that iPTF13asv has a stratified ejecta along the line of sight, with strong concentration of iron group elements near the center of the explosion.

5.2. iPTF13asv as an Intermediate Case between Normal and Super-Chandrasekhar Subclasses

In Table 4, we summarize a comparison of normal SNe, iPTF13asv, and super-Chandrasekhar SNe. As can be seen from the table, on the one hand, iPTF13asv shares similar light curve shapes and near-IR secondary peak with normal events. SNID also finds decent spectral matches between iPTF13asv and normal events. On the other hand, the peak radiation of iPTF13asv is as bright as super-Chandrasekhar events in both optical and UV. The evolution of Si II velocities of iPTF13asv is also similar to those of super-Chandrasekhar events. In addition, we derived an total ejecta mass slightly beyond the Chandrasekhar mass limit. Hence, we classify iPTF13asv as an intermediate case between normal and super-Chandrasekhar subclasses.

In addition to the features listed in the table, the H-band break, a sharp spectral feature formed by absorption of Fe II, Co II and Ni II (Hsiao et al. 2013), is also distinctive between super-Chandrasekhar and normal events. The H-band break emerges around the maximum for normal SNe and decays to disappear within a month of maximum. In contrast, this feature does not appear in the super-Chandrasekhar events. However, the only near-IR spectrum of iPTF13asv is taken one month after the maximum. Therefore, we cannot determine whether iPTF13asv shows the H-band break or not.

5.3. Progenitor

The massive ejecta and the stratification of the ejecta favor a DD progenitor system for iPTF13asv. In an SD system, a non-rotating WD cannot exceed the Chandrasekhar mass limit, and it is not clear in reality how

Table 4
Comparison of iPTF13asv to Normal and Super-Chandrasekhar SNe

Feature	Normal	iPTF13asv	Super-Chandrasekhar	Section ^a
B-band absolute peak magnitude	-18 – -19.5	-19.97 ± 0.06	< -19.6	§3.3
UV absolute peak magnitude	≥ -15	-15.25	≤ -15	§3.3 and Figure 7
B-band Δm_{15} (mag)	0.8 – 1.2	1.0	≈ 0.6	§3.3
Near-IR secondary peak	strong	strong	weak or absent	§3.3 and Figure 6
SNID	normal	normal	super-Chandrasekhar	§3.4.2 and Table 3
Carbon feature after max	no	weak	strong	§3.4.4 and Figures 10 and 11
Si II 6355 velocity at max (10^3 km s^{-1}) ^b	10 – 14	10	8 – 12	§3.4.3 and Figure 8
Si II 6355 velocity gradient at max ($\text{km s}^{-1} \text{ day}^{-1}$) ^b	50 – 150	~ 0	-72 – 46	§3.4.3 and Figure 9
⁵⁶ Ni mass (M_{\odot}) ^c	0.3 – 0.6	0.81 ^{+0.10} _{-0.18}	> 0.75	§4.2
Ejecta mass (M_{\odot}) ^c	0.8 – 1.5	1.59 ^{+0.45} _{-0.12}	> 1.5	§4.2

^a This column points to sections in this paper that discuss corresponding features

^b The velocity measurements of normal events are from Foley et al. (2011). Those of super-Chandrasekhar events are from Scalzo et al. (2012).

^c The mass measurements of normal events are from Scalzo et al. (2014b). Those of super-Chandrasekhar events are from Scalzo et al. (2012).

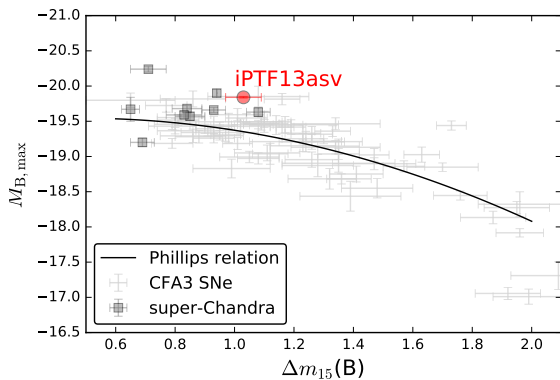


Figure 15. iPTF13asv is an outlier from the the Phillips relation. The Phillips relation is taken from Phillips et al. (1999). The CFA3 data are from Hicken et al. (2012). The super-Chandrasekhar events are from Scalzo et al. (2010) and Scalzo et al. (2012).

rotation could increase this mass limit. Hydrodynamic simulations (e.g., Kromer et al. 2010; Sim et al. 2013) also show that explosions in an SD system cannot avoid a certain level of mixing in the ejecta. Hence, these models do not easily concentrate most of the iron group elements in the center of the ejecta. For merging WDs, in contrast, simulations of prompt detonation (e.g., Moll et al. 2014) produce strongly stratified structures along polar directions in asymmetric ejecta. In these directions, iron group elements are confined to the low-velocity regions.

We also consider the core-degenerate scenario to explain the progenitor system of iPTF13asv (e.g., Soker et al. 2014), but more exploration in this scenario is needed to explain the weak mixing of iron group elements in the fast-moving ejecta, persistent carbon features after maximum, and low but almost constant Si II velocity.

5.4. iPTF13asv in cosmology

Unsurprisingly, iPTF13asv is an outlier from the Phillips relation (Phillips 1993). As shown in Figure 15, iPTF13asv is above the empirical relation by half a magnitude.

To have better calibration in cosmology, a third color term is introduced in the Phillips relation, i.e.,

$$\mu = m_B^* - (M_B - \alpha x_1 + \beta c), \quad (6)$$

where μ is the distance modulus; m_B^* is the observed

peak magnitude in the rest-frame B band; α , β and M_B are free parameters. To account for the dependence on the host galaxy properties, Sullivan et al. (2011) suggest to use different values of M_B for galaxies of stellar mass greater than and less than $10^{10} M_{\odot}$. In the case of iPTF13asv, the stellar mass of its host galaxy is $\sim 10^{7.8} M_{\odot}$. For galaxies with stellar mass less than $10^{10} M_{\odot}$, Betoule et al. (2014) used a fiducial value of $H_0 = 70 \text{ km s}^{-1} \text{ Mpc}^{-1}$ and obtained $M_B = -19.04 \pm 0.01$, $\alpha = 0.141 \pm 0.006$ and $\beta = 3.101 \pm 0.075$. Using the same H_0 and the iPTF13asv measurements of $m_B^* = 16.28 \pm 0.03$, $x_1 = 0.37 \pm 0.09$ and $c = -0.16 \pm 0.02$, we find that iPTF13asv can still be included in this empirical relation and thus be useful for cosmographic measurements, whereas super-Chandrasekhar events are outliers of this empirical relation (Scalzo et al. 2012).

5.5. UV-luminous SNe at High Redshifts

Spectroscopic classification for high-redshift SNe requires very long integration on big telescopes. Therefore, in high-redshift SN surveys, an optical-UV “dropout” is introduced to preselect type Ia candidates. For example, Riess et al. (2004, 2007) used the F850LP, F775W, and F606 filters on the *HST* Advanced Camera for Surveys (ACS) to search for SNe at redshifts up to 1.8.

The color preselection criteria may introduce bias by ignoring UV-luminous SNe. In Figure 16, we calculate the color difference in the F850LP, F775W, and F606 filters for normal SN1992a (Kirshner et al. 1993), near-UV blue SN2011fe (Mazzali et al. 2014), and UV-luminous iPTF13asv at different redshifts. As can be seen, the three SNe show different colors at high redshifts. Although the rate of iPTF13asv-like events is probably low in the nearby Universe, there might be more such SNe at high redshifts as there are more metal-poor dwarf galaxies at high redshifts. Hence it might become a non-negligible component in estimating the SN rate at high redshifts.

6. CONCLUSIONS

In this paper, we present multi-wavelength observations of a peculiar overluminous Type Ia supernova, iPTF13asv, discovered by the intermediate Palomar Transient Factory. Although its light curve shape ($\Delta m_{15} = 1.03 \pm 0.01 \text{ mag}$) and sharp secondary near-IR peak resemble characteristic features of normal Type

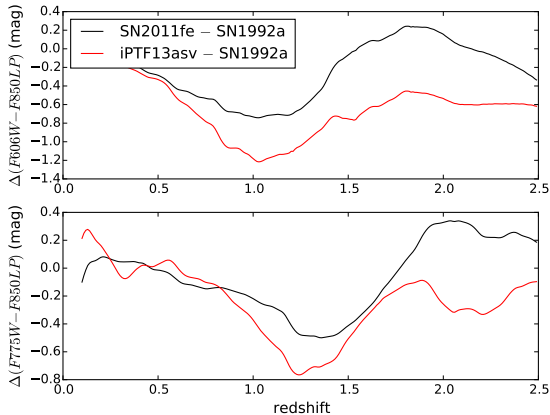


Figure 16. Color difference as a function of redshift for three different SNe Ia.

Ia supernovae, iPTF13asv shows low but almost constant expansion velocities and persistent carbon absorption features after the maximum, both of which are commonly seen in super-Chandrasekhar events. We derive a ^{56}Ni mass of $0.81^{+0.10}_{-0.18} M_{\odot}$ and a total ejecta mass of $1.59^{+0.45}_{-0.12} M_{\odot}$. Therefore, we suggest that iPTF13asv is an intermediate case between the normal and super-Chandrasekhar events.

Our observations of iPTF13asv also show an absence of iron absorption features in its early-phase spectra until several days before maximum and strong UV emission around peak. These observations, together with sharp near-IR secondary maxima, indicate that iPTF13asv has a stratified structure along the line of sight, with synthesized iron group elements concentrated in the center of its ejecta. Compared to hydrodynamic simulations, only WD mergers might produce the inferred ejecta structure. Therefore, based on the stratified ejecta and its similarity to super-Chandrasekhar events, we conclude that iPTF13asv originates from a double-degenerate progenitor system.

We speculate that iPTF13asv might represent a transition case between normal and super-Chandrasekhar events. The current and upcoming time-domain surveys, such as DECam surveys, Zwicky Transient Facility, and LSST, will find many more Type Ia supernovae of different subclasses. Equipped with fast-turnaround follow-up observations which allow us to estimate the ejecta mass and the ^{56}Ni mass, these surveys will map how spectral features (such as iron absorptions and carbon signatures) vary as a function of the total ejecta mass for supernovae. In particular, UV photometry and optical spectroscopy of these supernovae at early phases will reveal information about mixing of iron group elements. Understanding peculiar but possibly linking events like iPTF13asv in the context of large samples will further our knowledge about different subtypes of Type Ia supernovae and their physical origins.

We thank the anonymous referee for very useful comments and suggestions that substantially improved the manuscript. We are also grateful to M. Kromer for useful discussion about theoretic progenitor scenarios, and to A. De Cia, O. Yaron, D. Tal, D. Perley, K. Tinianont,

A. Waszczak, I. Arcavi, and S. Tang for performing observations and data reduction.

This research is partly supported by the *Swift* Guest Investigator program and by the National Science Foundation. Y.C. and M.M.K. acknowledge support from the National Science Foundation PIRE program grant 1545949. A.G. and R.A. acknowledge support from the Swedish Research Council and the Swedish Space Board. E.Y.H. acknowledges the support provided by the Danish Agency for Science and Technology and Innovation through a Sapere Aude Level 2 grant.

Some observations obtained with the SuperNova Integral Field Spectrograph on the University of Hawaii 2.2-m telescope as part of the Nearby Supernova Factory II project, a scientific collaboration between the Centre de Recherche Astronomique de Lyon, Institut de Physique Nucléaire de Lyon, Laboratoire de Physique Nucléaire et des Hautes Energies, Lawrence Berkeley National Laboratory, Yale University, University of Bonn, Max Planck Institute for Astrophysics, Tsinghua Center for Astrophysics, and Centre de Physique des Particules de Marseille.

Some data were obtained with ALFOSC, which is provided by the Instituto de Astrofísica de Andalucía (IAA) under a joint agreement with the University of Copenhagen and NOTSA.

We also thank the RATIR project team and the staff of the Observatorio Astronómico Nacional on Sierra San Pedro Mártir. RATIR is a collaboration between the University of California, the Universidad Nacional Autónoma de México, NASA Goddard Space Flight Center, and Arizona State University, benefiting from the loan of an H2RG detector and hardware and software support from Teledyne Scientific and Imaging. RATIR, the automation of the Harold L. Johnson Telescope of the Observatorio Astronómico Nacional on Sierra San Pedro Mártir, and the operation of both are funded through NASA grants NNX09AH71G, NNX09AT02G, NNX10AI27G, and NNX12AE66G, CONACyT grants LN 260369, and UNAM PAPIIT grant IG100414.

A portion of this work was carried out at the Jet Propulsion Laboratory, California Institute of Technology, under a contract with the National Aeronautics and Space Administration. Copyright 2016 California Institute of Technology. All Rights Reserved. US Government Support Acknowledged.

REFERENCES

- Aldering, G., Antilogus, P., Bailey, S., et al. 2006, *ApJ*, 650, 510
 Barone-Nugent, R. L., Lidman, C., Wyithe, J. S. B., et al. 2012, *MNRAS*, 425, 1007
 Betoule, M., Kessler, R., Guy, J., et al. 2014, *A&A*, 568, A22
 Blondin, S., & Tonry, J. L. 2007, *ApJ*, 666, 1024
 Blondin, S., Matheson, T., Kirshner, R. P., et al. 2012, *AJ*, 143, 126
 Breeveld, A. A., Landsman, W., Holland, S. T., et al. 2011, in *American Institute of Physics Conference Series*, Vol. 1358, American Institute of Physics Conference Series, ed. J. E. McEnery, J. L. Racusin, & N. Gehrels, 373–376
 Brown, P. J. 2014, *ApJ*, 796, L18
 Brown, P. J., Dawson, K. S., de Pasquale, M., et al. 2012, *ApJ*, 753, 22
 Brown, P. J., Kuin, P., Scalzo, R., et al. 2014, *ApJ*, 787, 29
 Burns, C. R., Stritzinger, M., Phillips, M. M., et al. 2014, *ApJ*, 789, 32
 Cao, Y., Kulkarni, S. R., Howell, D. A., et al. 2015, *Nature*, 521, 328

- Cenko, S. B., Fox, D. B., Moon, D.-S., et al. 2006, *PASP*, 118, 1396
- Denicoló, G., Terlevich, R., & Terlevich, E. 2002, *MNRAS*, 330, 69
- Di Stefano, R., Voss, R., & Claeys, J. S. W. 2011, *ApJ*, 738, L1
- Filippenko, A. V., Richmond, M. W., Matheson, T., et al. 1992, *ApJ*, 384, L15
- Firth, R. E., Sullivan, M., Gal-Yam, A., et al. 2015, *MNRAS*, 446, 3895
- Fitzpatrick, E. L. 1999, *PASP*, 111, 63
- Foley, R. J., McCully, C., Jha, S. W., et al. 2014, *ApJ*, 792, 29
- Foley, R. J., Sanders, N. E., & Kirshner, R. P. 2011, *ApJ*, 742, 89
- Foster, C., Hopkins, A. M., Gunawardhana, M., et al. 2012, *A&A*, 547, A79
- Garavini, G., Folatelli, G., Goobar, A., et al. 2004, *AJ*, 128, 387
- Goobar, A., & Leibundgut, B. 2011, *Annual Review of Nuclear and Particle Science*, 61, 251
- Goobar, A., Kromer, M., Siverd, R., et al. 2015, *ApJ*, 799, 106
- Guy, J., Astier, P., Baumont, S., et al. 2007, *A&A*, 466, 11
- Hachisu, I., Kato, M., & Nomoto, K. 2012, *ApJ*, 756, L4
- Hicken, M., Garnavich, P. M., Prieto, J. L., et al. 2007, *ApJ*, 669, L17
- Hicken, M., Challis, P., Kirshner, R. P., et al. 2012, *ApJS*, 200, 12
- Hoeflich, P., & Khokhlov, A. 1996, *ApJ*, 457, 500
- Howell, D. A., Sullivan, M., Perrett, K., et al. 2005, *ApJ*, 634, 1190
- Howell, D. A., Sullivan, M., Nugent, P. E., et al. 2006, *Nature*, 443, 308
- Hsiao, E. Y., Conley, A., Howell, D. A., et al. 2007, *ApJ*, 663, 1187
- Hsiao, E. Y., Marion, G. H., Phillips, M. M., et al. 2013, *ApJ*, 766, 72
- Jeffery, D. J. 1999, *ArXiv Astrophysics e-prints*, astro-ph/9907015
- Jeffery, D. J., Branch, D., & Baron, E. 2006, *ArXiv Astrophysics e-prints*, astro-ph/0609804
- Justham, S. 2011, *ApJ*, 730, L34
- Kasen, D. 2006, *ApJ*, 649, 939
- . 2010, *ApJ*, 708, 1025
- Kelly, P. L., Fox, O. D., Filippenko, A. V., et al. 2014, *ApJ*, 790, 3
- Kennicutt, Jr., R. C. 1998, *ARA&A*, 36, 189
- Kirshner, R. P., Jeffery, D. J., Leibundgut, B., et al. 1993, *ApJ*, 415, 589
- Kriek, M., van Dokkum, P. G., Labbé, I., et al. 2009, *ApJ*, 700, 221
- Krisciunas, K., Hastings, N. C., Loomis, K., et al. 2000, *ApJ*, 539, 658
- Kromer, M., Sim, S. A., Fink, M., et al. 2010, *ApJ*, 719, 1067
- Kushnir, D., Katz, B., Dong, S., Livne, E., & Fernández, R. 2013, *ApJ*, 778, L37
- Lantz, B., Aldering, G., Antilogus, P., et al. 2004, in *Society of Photo-Optical Instrumentation Engineers (SPIE) Conference Series*, Vol. 5249, *Optical Design and Engineering*, ed. L. Mazuray, P. J. Rogers, & R. Wartmann, 146–155
- Law, N. M., Kulkarni, S. R., Dekany, R. G., et al. 2009, *PASP*, 121, 1395
- Li, W., Bloom, J. S., Podsiadlowski, P., et al. 2011, *Nature*, 480, 348
- Lundqvist, P., Nyholm, A., Taddia, F., et al. 2015, *A&A*, 577, A39
- Maeda, K., & Iwamoto, K. 2009, *MNRAS*, 394, 239
- Maoz, D., Mannucci, F., & Nelemans, G. 2014, *ARA&A*, 52, 107
- Margutti, R., Parrent, J., Kamble, A., et al. 2014, *ApJ*, 790, 52
- Marion, G. H., Brown, P. J., Vinkó, J., et al. 2016, *ApJ*, 820, 92
- Matheson, T., Kirshner, R. P., Challis, P., et al. 2008, *AJ*, 135, 1598
- Mazzali, P. A., Danziger, I. J., & Turatto, M. 1995, *A&A*, 297, 509
- Mazzali, P. A., Sullivan, M., Hachinger, S., et al. 2014, *MNRAS*, 439, 1959
- McCully, C., Jha, S. W., Foley, R. J., et al. 2014, *Nature*, 512, 54
- Milne, P. A., Brown, P. J., Roming, P. W. A., Bufano, F., & Gehrels, N. 2013, *ApJ*, 779, 23
- Moll, R., Raskin, C., Kasen, D., & Woosley, S. E. 2014, *ApJ*, 785, 105
- Nadyozhin, D. K. 1994, *ApJS*, 92, 527
- Nobili, S., & Goobar, A. 2008, *A&A*, 487, 19
- Nomoto, K., & Iben, Jr., I. 1985, *ApJ*, 297, 531
- Nugent, P., Kim, A., & Perlmutter, S. 2002, *PASP*, 114, 803
- Nugent, P. E., Sullivan, M., Cenko, S. B., et al. 2011, *Nature*, 480, 344
- Oke, J. B., & Gunn, J. E. 1982, *PASP*, 94, 586
- Pan, Y.-C., Sullivan, M., Maguire, K., et al. 2014, *MNRAS*, 438, 1391
- Parrent, J. T., Thomas, R. C., Fesen, R. A., et al. 2011, *ApJ*, 732, 30
- Patat, F., Chandra, P., Chevalier, R., et al. 2007, *Science*, 317, 924
- Pereira, R., Thomas, R. C., Aldering, G., et al. 2013, *A&A*, 554, A27
- Phillips, M. M. 1993, *ApJ*, 413, L105
- Phillips, M. M., Lira, P., Suntzeff, N. B., et al. 1999, *AJ*, 118, 1766
- Piro, A. L. 2008, *ApJ*, 679, 616
- . 2012, *ApJ*, 759, 83
- Piro, A. L., & Morozova, V. S. 2015, *ArXiv e-prints*, arXiv:1512.03442
- Poznanski, D., Prochaska, J. X., & Bloom, J. S. 2012, *MNRAS*, 426, 1465
- Rau, A., Kulkarni, S. R., Law, N. M., et al. 2009, *PASP*, 121, 1334
- Riess, A. G., Strolger, L.-G., Tonry, J., et al. 2004, *ApJ*, 600, L163
- Riess, A. G., Strolger, L.-G., Casertano, S., et al. 2007, *ApJ*, 659, 98
- Saio, H., & Nomoto, K. 2004, *ApJ*, 615, 444
- Scalzo, R., Aldering, G., Antilogus, P., et al. 2012, *ApJ*, 757, 12
- . 2014a, *MNRAS*, 440, 1498
- Scalzo, R. A., Ruiter, A. J., & Sim, S. A. 2014b, *MNRAS*, 445, 2535
- Scalzo, R. A., Aldering, G., Antilogus, P., et al. 2010, *ApJ*, 713, 1073
- Scalzo, R. A., Childress, M., Tucker, B., et al. 2014c, *MNRAS*, 445, 30
- Schlafly, E. F., & Finkbeiner, D. P. 2011, *ApJ*, 737, 103
- Shappee, B. J., Stanek, K. Z., Pogge, R. W., & Garnavich, P. M. 2013, *ApJ*, 762, L5
- Silverman, J. M., & Filippenko, A. V. 2012, *MNRAS*, 425, 1917
- Silverman, J. M., Ganeshalingam, M., Li, W., et al. 2011, *MNRAS*, 410, 585
- Sim, S. A., Seitzzahl, I. R., Kromer, M., et al. 2013, *MNRAS*, 436, 333
- Soker, N., García-Berro, E., & Althaus, L. G. 2014, *MNRAS*, 437, L66
- Stanishev, V., Goobar, A., Amanullah, R., et al. 2015, *ArXiv e-prints*, arXiv:1505.07707
- Sternberg, A., Gal-Yam, A., Simon, J. D., et al. 2014, *MNRAS*, 443, 1849
- Sullivan, M., Guy, J., Conley, A., et al. 2011, *ApJ*, 737, 102
- Swartz, D. A., Sutherland, P. G., & Harkness, R. P. 1995, *ApJ*, 446, 766
- Taubenberger, S., Benetti, S., Childress, M., et al. 2011, *MNRAS*, 412, 2735
- Thomas, R. C., Nugent, P. E., & Meza, J. C. 2011a, *PASP*, 123, 237
- Thomas, R. C., Aldering, G., Antilogus, P., et al. 2011b, *ApJ*, 743, 27
- Vinkó, J., Sárneczky, K., Takáts, K., et al. 2012, *A&A*, 546, A12
- Walker, M. G., Mateo, M., Olszewski, E. W., et al. 2007, *ApJ*, 667, L53
- Whelan, J., & Iben, Jr., I. 1973, *ApJ*, 186, 1007
- Wolf, R. C., D'Andrea, C. B., Gupta, R. R., et al. 2016, *ApJ*, 821, 115
- Yamanaka, M., Kawabata, K. S., Kinugasa, K., et al. 2009, *ApJ*, 707, L118
- Yaron, O., & Gal-Yam, A. 2012, *PASP*, 124, 668
- Yoon, S.-C., & Langer, N. 2004, *A&A*, 419, 623
- . 2005, *A&A*, 435, 967
- Yuan, F., Quimby, R. M., Wheeler, J. C., et al. 2010, *ApJ*, 715, 1338
- Zhou, L., Wang, X., Zhang, K., et al. 2013, *Central Bureau Electronic Telegrams*, 3543, 1